

Link to Densify: Topological Transition During the Compression of Amorphous Ices

Yair Augusto Gutiérrez Fosado,¹ Davide Michieletto,^{1,2} and Fausto Martelli^{3,4}

¹*School of Physics and Astronomy, University of Edinburgh,
Peter Guthrie Tait Road, Edinburgh, EH9 3FD, UK**

²*MRC Human Genetics Unit, Institute of Genetics and Cancer,
University of Edinburgh, Edinburgh EH4 2XU, UK*

³*BM Research Europe, Hartree Centre, Daresbury WA4 4AD, UK*

⁴*Department of Chemical Engineering, University of Manchester, Manchester M13 9PL, UK†*

In this work we study the structural and topological transition between amorphous ices. We discover that applying external pressure to low-density amorphous ice (LDA) distorts the looped motifs constituting the hydrogen bond network (HBN). The transition to high-density amorphous ice (HDA) is accompanied by an abrupt topological transition of the HBN, which starts to display interpenetrated and Hopf linked looped motifs. This topologically linked HBN is metastable during decompression, and the links disentangle through a first order transition at the critical point. We discover that the rearrangement of the HBN motifs at the transitions induce a loss of mechanical rigidity, dramatically increasing compressibility. We argue that topological transitions may be a generic mechanism for the densification of network-forming amorphous materials and enriches our understanding of the properties of water.

Water's distinctive molecular geometry and the capacity to form flexible hydrogen bonds (HBs), results in an extraordinarily intricate phase diagram encompassing, at least, 20 crystalline states [1], two liquid forms [2–6], and several amorphous phases [7] including the low-density amorphous ice (LDA) and the high-density amorphous ice (HDA). The hydrogen bond network (HBN) of LDA is mostly dominated by hexagonal motifs (or loops) and is insensitive to the applied pressure [8]. The stability of the network topology has been linked to the emergence of physical properties in several materials, including the suppression of long-range density fluctuations in glassy water [9], to the vitrification of liquid water under electric fields [10], and the fragility of a wide range of silicate glasses [11]. When pressure is applied isotropically to LDA, the HBN structure does not change considerably until a critical pressure P_c^* is reached. At this critical pressure, the HBN undergoes a substantial rearrangement. The demarcation line separating LDA and HDA seems to be of the first-order-kind [12]. Despite multiple efforts, a full understanding of the mechanism(s) underlying this phase transition is still lacking, and it is the focus of our work. We perform classical molecular dynamics (MD) simulations of the isothermal compression/decompression of amorphous ices along several isotherms. We look for non-trivial topological motifs embedded in the HBN of amorphous ices and previously found in liquid water described with the same water model [6]. We discover that the transition during compression between LDA and HDA is demarcated by the onset of a percolating HBN made of interpenetrated and Hopf linked looped motifs, which are metastable during decompression. Our results unveil the kinetics of transformation between amorphous ices, fully explain their interconversion, and offer a topological explanation for the singular behavior of the isothermal compressibility. More

broadly, our results provide a picture that may be the general mechanism of densification in network-forming amorphous materials.

RESULTS AND DISCUSSIONS

We perform classic MD simulations of the TIP4P/2005 model at temperatures $T=100, 120,$ and 140 K and spanning a range of pressures (see SI). We identify hydrogen bonds (HB) by looking for molecules that are closer than 3.5 Å and whose angle formed between O-H-O is smaller than 30° [13]. We then produce a graph where each vertex is a water molecule and each edge represents a HB (Fig. 1A). This water model is well known to undergo phase transitions during compression/decompression at around 0.8 and -0.4 GPa, respectively [7]. At these critical points, the average density displays an abrupt transition (Fig. 1B). To characterize the structure of the HBN during the transition we look for loops in the graph as closed paths with no repetition of vertices or edges other than the starting and endpoints. We compute all the loops $(N_{i,l})$ formed by $l \in [3, l_m]$ water molecules, passing through the i th-vertex in the graph, $i \in [1, M = 512]$. We search for loops made at most by $l_m = 13$ molecules [6] for computational feasibility (see SI for more details). The system has then $N_{loops} = \sum_{i=1}^M N_{i,l}$. In fig. 1(C) we report the average number of loops $\langle N_{loops} \rangle$ as a function of the applied pressure at $T = 100$ K during compression/decompression. In LDA, $\langle N_{loops} \rangle$ fluctuates around $\langle N_{loops} \rangle \simeq 3.8 \times 10^4$. This indicates that the HBN of LDA is mostly insensitive to this range of pressures [8, 9]. A sudden drop to $\langle N_{loops} \rangle \simeq 3.2 \times 10^4$ occurs at $P_c^* \simeq 0.8$ GPa, signaling the transition to HDA. Upon increasing further the pressure, the HBN is characterized by larger fluctuations of $\langle N_{loops} \rangle$, reflecting the sen-

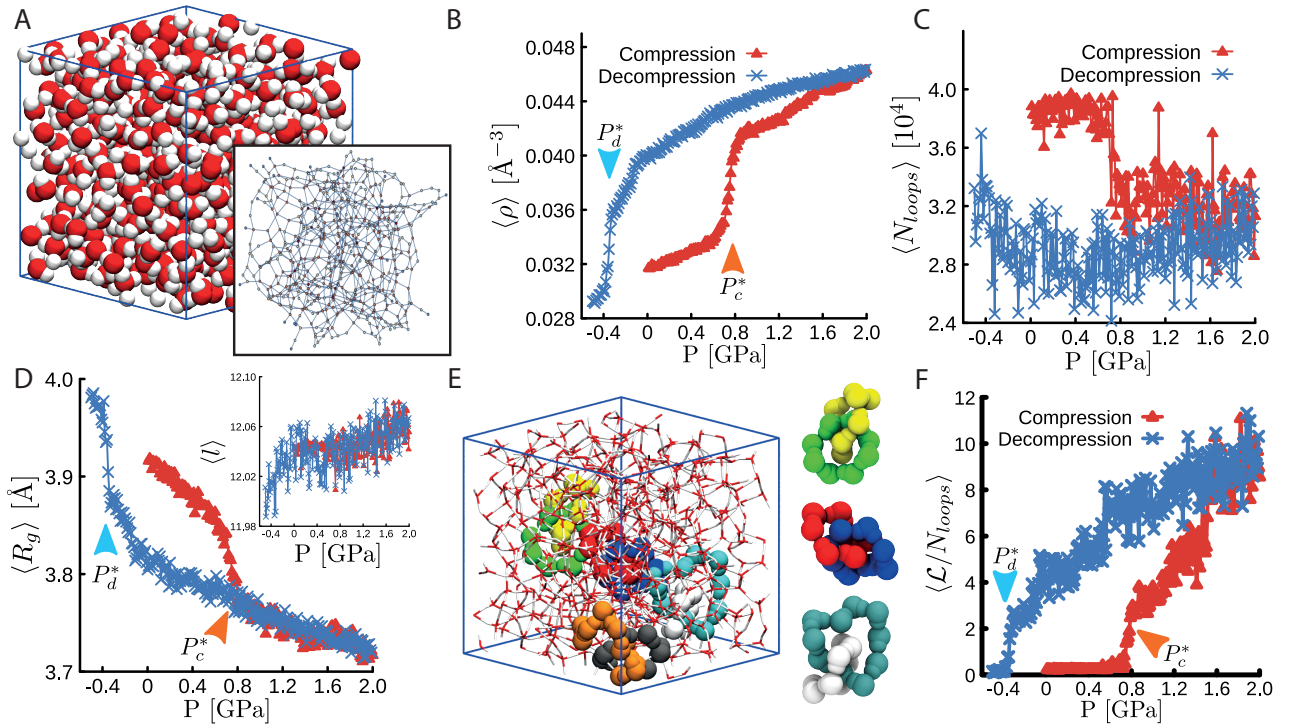


Figure 1. Data obtained at $T=100$ K. (A) Snapshot of the simulation box and (inset) corresponding graph representation of the HBN. (B) Average density as a function of applied pressure. (C) The number of loops within the HBN (with a length shorter than 13 water molecules). (D) The average radius of gyration of the loops. (inset) Average length of the loops. (E) Snapshot of a simulation of HDA at 1 GPa where three pairs of Hopf-linked loops are highlighted. (F) Average valence, i.e. number of loops linked to any one loop within the HBN. Data points during compression (decompression) are reported as red (blue).

sitivity to the increased pressure [8]. The decompression of HDA shows an initial decrease in $\langle N_{loops} \rangle$ which can be attributed to the slower relaxation time of the HBN compared to the increased available volume. Eventually, $\langle N_{loops} \rangle$ increases reaching $\langle N_{loops} \rangle \simeq 3.2 \times 10^4$ at the lowest negative pressure, emphasizing the hysteresis cycle typical of first-order phase transitions. Interestingly, the number density of loops $\langle N_{loops} / L^3 \rangle$ is roughly constant around 2.5-3 through the compression/decompression, indicating a significant structural rearrangement of the loops within the HBN (see SI). In fig. 1(D) we report the average radius of gyration $\langle R_g \rangle$ computed over all loops during compression/decompression. The applied pressure rapidly decreases $\langle R_g \rangle$ in LDA and indicates that the loops in the HBN become increasingly smaller without changing the overall structure [8]. At the critical P_c^* , the behavior of $\langle R_g \rangle$ undergoes a sudden change in trend. Upon decompression, the small size of the loops appears metastable and returns to the original size only after at the critical P_d^* once again displaying a remarkable hysteresis cycle. We should note that despite the reduction in $\langle R_g \rangle$ during compression, the *length* of the loops steadily increases (see fig. 1D, inset), which is in seeming contradiction with the behaviour of $\langle R_g \rangle$.

Inspired by recent work on the appearance of topological motifs in liquid water [6] and DNA hydrogels [14], we decided to look for non-trivial topological motifs in our

systems. To do this, we computed the linking number Lk between pairs of closed-oriented curves γ_i and γ_j through the Gauss integral

$$Lk(\gamma_i, \gamma_j) = \frac{1}{4\pi} \oint_{\gamma_i} \oint_{\gamma_j} \frac{(\mathbf{r}_j - \mathbf{r}_i)}{|\mathbf{r}_j - \mathbf{r}_i|^3} \cdot (d\mathbf{r}_j \times d\mathbf{r}_i), \quad (1)$$

where \mathbf{r}_i and \mathbf{r}_j are the vectors defining the position of all the points (the vertices on the graph) along the curves (the edges on the graph) γ_i and γ_j , respectively. Examples of such topological links within the HBN are shown in Fig. 1E. Since the orientation of the loops is randomly assigned, the value of Lk averaged over all the pairs of loops is close to zero. To compute the overall degree of linking within the HBN, we thus compute the total number of times that two loops are linked regardless of the sign of Lk , i.e. $\mathcal{L} = \sum_{i>j}^{N_{loops}} |Lk(\gamma_i, \gamma_j)|$. We do not observe loops with $|Lk| > 1$, nor any appreciable number of other complex topologies, such as knots (see SI).

The behavior of \mathcal{L} , scaled by the average number of loops in the HBN is reported in Fig. 1F. A complete absence of links characterizes LDA. Simple interlinked motifs, i.e. Hopf links ($\mathcal{L} = 1$, Fig. 1E) appear at the transition to HDA. Thus, P_c^* marks the stability limit of the LDA, above which the network's configurational entropy increases thanks to the interlinking, via Hopf links, of otherwise independent looped motifs. Upon increasing the applied pressure beyond P_c^* , the size of the loops

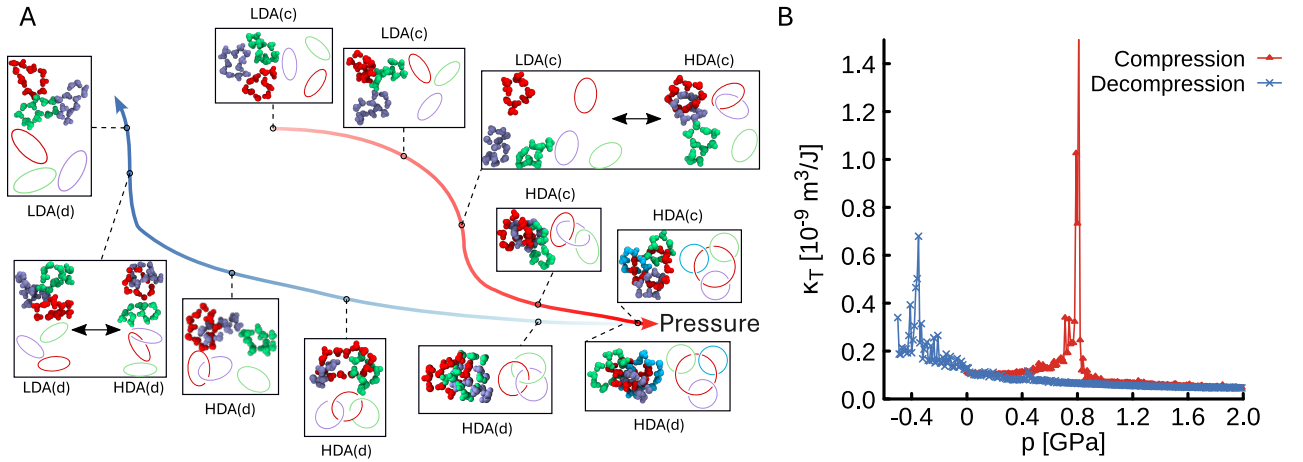


Figure 2. (A) Pictorial representation of the HBN rearrangement during compression and decompression of amorphous ices. Snapshots of loops within the HBN are shown along the curves. (B) Profile of the isothermal compressibility k_T computed at $T = 100$ K during compression (red symbols) and decompression (blue symbols).

$\langle R_g \rangle$ slowly decreases while $\langle \mathcal{L}/N_{loops} \rangle$ rapidly increases (fig. 1D-F), thus increasing the valence, or the number of loops that are linked to any one loop. The fast increase in linking between loops and the slow decrease in their size indicates that the increase in topological complexity of the HBN becomes the dominant mechanism allowing the increase in density. Decompression of HDA induces an increase of $\langle R_g \rangle$ (fig. 1D) accompanied by a slow reduction of $\langle \mathcal{L}/N_{loops} \rangle$ (fig. 1F). In turn, this suggests that the links between the loops are stable, yet the loops are less distorted. At the decompression critical pressure, P_d^* , $\langle R_g \rangle$ undergoes a sudden jump concurrently with a sudden drop in $\langle \mathcal{L}/N_{loops} \rangle$. The increasing available space, therefore, allows for a complete disentanglement of the loops within the HBN.

The emerging picture can be summarized as follows (see Fig. 2A): in LDA the isotropic pressure shrinks the loops of the HBN and once the critical pressure is reached, the transition to HDA is characterized by the abrupt appearance of non-trivial topological linking which then increases with pressure. At negative pressures, the recovery of LDA is induced by the full disentanglement of the HBN motifs. At the transition, there is an equilibrium between linked and unlinked loop topologies. Importantly, the sudden entanglement occurring during the phase transition from LDA to HDA (and viceversa during decompression) have measurable effects on the physical properties of the systems. In Fig. 2B we report the isothermal compressibility k_T , computed during compression and decompression at $T=100$ K, and displaying a singular behaviour in correspondence with the phase transitions. During compression, the divergence of k_T is caused by the loops transiently opening and reforming in a different, Hopf linked, interpenetrated configuration. The latter can accommodate more molecules per unit volume, and is thus accompanied by an abrupt increase

in compressibility, leading to an increase density and, in parallel, by a reduction of the number loops (maintaining the loop number density roughly constant through the transition, see SI). At pressures higher than P_c^* the HBN displays stable Hopf linked and interpenetrated loops, thus re-establishing rigidity to the system. During the decompression, the increase in k_T is caused by the momentary opening of the loops to allow water molecules to disentangle, occupying the increased available space. The opening of the loops to allow for the creation and the resolution of Hopf linked loops also explains the observed loss of hyperuniformity in these samples [8, 15].

The HBN of LDA and HDA are markedly similar to those of their corresponding liquid phases close to the critical point [6], supporting the conjectured existence of a liquid-liquid critical point for this water model and the suggestion that LDA and HDA may be the glassy states of the equilibrium liquids [16]. The recently reported medium-density amorphous (MDA) [17, 18], should be investigated in terms of the complex topological motifs inspected in this work and in Ref. [6]. Our results and the structural similarities recently found between some of the MDAs and LDA [19] suggest that MDAs may correspond to LDA or HDA configurations with distorted or interpenetrating HBNs.

Our study explains the topological nature and origin of the hysteresis cycle between amorphous ices and the first-order phase transition separating them. The network's topological re-arrangement uncovered in this work may be a general mechanism of densification in amorphous network-forming materials at large, including semiconductors and pharmaceuticals. Despite its complexity, the HBN topology of HDA creates mostly incompressible configurations at the limit of nearly hyperuniformity [8, 15]. Unveiling the intricacies of this network adds a dimension to the realization of disordered hyper-

uniform materials.

CODE AVAILABILITY

Trajectories and analysis codes are available at: <https://git.ecdf.ed.ac.uk/ygutier2/amorphous-ice-topology>

ACKNOWLEDGEMENTS

F.M. acknowledges support from the Hartree National Centre for Digital Innovation, a collaboration between STFC and IBM. DM acknowledges the Royal Society and the European Research Council (grant agreement No 947918, TAP) for funding. The authors also acknowledge the contribution of the COST Action Eutopia, CA17139. For the purpose of open access, the author has applied a Creative Commons Attribution (CC BY) licence to any Author Accepted Manuscript version arising from this submission.

* yair.fosado@ed.ac.uk

† fausto.martelli@ibm.com

- [1] C. G. Salzmann, *J. Chem. Phys.* **150**, 060901 (2019).
- [2] J. C. Palmer, F. Martelli, Y. Liu, R. Car, A. Z. Panagiotopoulos, and P. G. Debenedetti, *Nature* **510**, 385 (2014).
- [3] P. G. Debenedetti, F. Sciortino, and G. H. Zerze, *Science* **369**, 289 (2020).
- [4] K. H. Kim, A. Späh, H. Pathak, F. Perakis, D. Mariedahl, K. Amann-Winkel, J. A. Sellberg, J. H. Lee, S. Kim, J. Park, K. H. Nam, T. Katayama, and A. Nilsson, *Science* **358**, 1589 (2017).
- [5] J. Sellberg, H. C., T. A. McQueen, H. L. N. D. Loh, D. Schlesinger, R. G. Sierra, D. Nordlund, C. Y. Hampton, S. D., D. D. P., B. M., C. C., M. A. V., B. A., W. K. T., W. T. M., C. C., F. J., S. L. B., S. M. M., M. M., W. G. J., B. S., P. L. G. M., B. M. J., and N. A., *Nature* **510**, 381 (2014).
- [6] A. Neophytou, D. Chakrabarti, and F. Sciortino, *Nature Physics* **18**, 1248 (2022).
- [7] K. Amann-Winkel, R. Böhmer, F. Fujara, C. Gainaru, B. Geil, and T. Loerting, *Rev. Mod. Phys.* **88**, 011002 (2016).
- [8] M. Formanek, S. Torquato, R. Car, and F. Martelli, *J. Phys. Chem. B* **127**, 3946 (2023).
- [9] F. Martelli, *PNAS Nexus* **1**, pgac090 (2022).
- [10] G. Cassone and F. Martelli, *Nat. Commun.* **15**, 1856 (2024).
- [11] Y. Shi, B. Deng, O. Gulbiten, M. Bauchy, Q. Zhou, J. Neufeind, S. R. Elliott, N. J. Smith, and D. C. Allan, *Nat. Commun.* **14**, 13 (2023).
- [12] O. Mishima, L. Calvert, and E. Whalley, *Nature* **324**, 76 (1985).
- [13] A. Luzar and D. Chandler, *Nature* **379**, 55 (1996).
- [14] G. Palombo, S. Weir, D. Michieletto, and Y. A. G. Fosado, “Topological elasticity in physical gels with limited valence,” (2023), arXiv:2308.09689 [cond-mat.soft].
- [15] F. Martelli, S. Torquato, N. Giovambattista, and R. Car, *Phys. Rev. Lett.* **119**, 136002 (2017).
- [16] F. Martelli, F. Leoni, F. Sciortino, and J. Russo, *J. Chem. Phys.* **153** (2020).
- [17] A. Rosu-Finsen, M. B. Davies, A. Amon, H. Wu, A. Sella, A. Michaelides, and C. G. Salzmann, *Science* **379**, 474 (2023).
- [18] A. Eltareb, G. E. Lopez, and N. Giovambattista, *Communications Chemistry* **7**, 36 (2024).
- [19] Z. Faure Beaulieu, V. L. Deringer, and F. Martelli, *J. Chem. Phys.* **160** (2024).
- [20] J. L. F. Abascal and C. Vega, *J. Chem. Phys.* **123**, 234505 (2005).
- [21] M. J. Abraham, T. Murtola, R. Schulz, S. Páll, J. C. Smith, B. Hess, and E. Lindahl, *SoftwareX* **1**, 19 (2015).
- [22] J. Wong, D. A. Jahn, and N. Giovambattista, *J. Chem. Phys.* **143** (2015).
- [23] F. Martelli, N. Giovambattista, S. Torquato, and R. Car, *Physical Review Materials* **2**, 075601 (2018).
- [24] S. Nosé, *Mol. Phys.* **52**, 255 (1984).
- [25] W. G. Hoover, *Phys. Rev. A* **31**, 1695 (1985).
- [26] H. J. Berendsen, J. v. Postma, W. F. Van Gunsteren, A. DiNola, and J. R. Haak, *J. Chem. Phys.* **81**, 3684 (1984).
- [27] W. C. Swope, H. C. Andersen, P. H. Berens, and K. R. Wilson, *J. Chem. Phys.* **76**, 637 (1982).
- [28] L. Tubiana, G. Polles, E. Orlandini, and C. Micheletti, *The European physical journal E* **41**, 1 (2018).

SUPPLEMENTARY INFORMATION

MOLECULAR DYNAMICS SIMULATIONS

Classical molecular dynamics simulations were performed on $N = 512$ rigid water molecules described by the TIP4P/2005 interaction potential [20] in the isobaric (NPT) ensemble using the GROMACS 2021.5 package [21]. The TIP4P/2005 water model reproduces well the phase diagram of water at the thermodynamic conditions of interest of this work [22, 23]. Coulombic and Lennard-Jones interactions were calculated with a cutoff distance of 1.1 nm and long-range electrostatic interactions were treated using the Particle-Mesh Ewald (PME) algorithm. Temperatures and pressures are controlled using the Nosé-Hoover thermostat [24, 25] with a constant of 0.2 ps, and the Berendsen barostat [26] with a time constant of 1 ps. Equations of motions are integrated with the Verlet algorithm [27] with a time step of 1 fs. The simulation protocol follows previous works employing the same water model [15, 22, 23]. LDA configurations were obtained by cooling liquid water equilibrated at $T=300$ K with a quenching rate of 1 K/ns down to $T=100$ K. Compression/decompression cycles were simulated with a compression/decompression rate of 0.01 GPa/ns at $T=100$ K, $T=120$ K and $T=140$ K. The highest pressure simulated was 2 GPa, the lowest was -0.5 GPa.

LINKS AND KNOTS

To improve the efficiency of our analysis, after identifying all the $N_{i,l}$ loops involving a vertex i , we remove that vertex and continue our search at vertex $i+1$. To prevent the identification of linear paths as loops (closed through the periodic boundary conditions), we use the minimum image criterion (MIC) to reconstruct the loops, and we impose the condition on each loop's radius of gyration $R_g < L/3$, with $R_g^2 = \frac{1}{l} \sum_{n=1}^l [\mathbf{r}_{\text{mean}} - \mathbf{r}_n]^2$. In this relation, \mathbf{r}_n , \mathbf{r}_{mean} and l represent the position of the n -th oxygen forming the loop, the center of mass of the loop and its size, respectively. In Fig. S1 we report the density of loops as function of the pressure. We note that on average the density of loops is conserved (also at the transition pressures $P_c^* = 0.8$ GPa and $P_d^* = -0.4$ GPa)

The identification of knotted states of individual loops (performed by using KymoKnot [28]), requires the use of longer loops than the computation of the linking \mathcal{L} . Our analysis revealed that at our highest pressure (2 GPa), knots could only be found when $l_{\text{max}} \geq 21$. In fact, for $l_{\text{max}} = 21$ we identified a total of $\sim 2 \times 10^7$ loops and only 4 knots (all of them trefoils). Therefore, the average number of knots per loop is considerably smaller than the average number of links per loop.

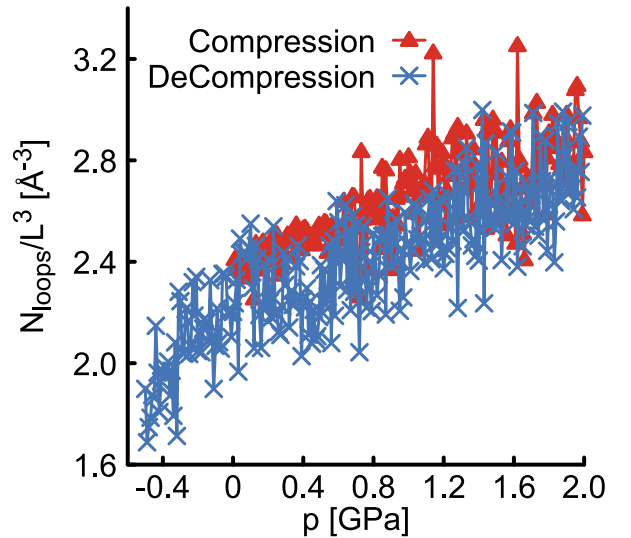


Figure S1. Density of loops (N_{loops}/L^3 , with L the box size) as function of the pressure at $T=100$ K. During compression $N_{\text{loops}}/L^3 \in [2.2, 3.0]^{-3}$, while during decompression $N_{\text{loops}}/L^3 \in [1.6, 2.8]^{-3}$

Although it was possible to find knots at $P = 2$ GPa when $l_{\text{max}} = 21$, this was not enough to capture the discontinuity in the number of knots as a function of the pressure, that is expected to mark the transition between the low density and high density amorphous-ice. Therefore, it is necessary to increase the value of l_{max} . However, because the number of loops increases exponentially with l_{max} , the analysis becomes computationally expensive and unfeasible for $l_{\text{max}} > 21$. One possible way to overcome this technical issue is by finding only rings made of exactly (and not up-to) $l^* = 25$ water molecules. In addition, we set to 500'000 as the maximum number of rings that our algorithm can find passing through a single vertex in the graph. With these two conditions we computed the number of knots (N_{knots}) as function of the pressure reported by the red data points in Fig. S2(b), when the system is under compression. In this plot we can identify the critical pressure ($P_c = 0.8$ GPa) at which the system undergoes a change in its topological state (from unknotted to knotted), but the analysis does not provide a full description about the knotting probability of the system. Analogous results during decompression are reported by the blue data points in Fig S2(b, right), where we identify $P_d = -0.4$ GPa, in agreements with the transition observed with \mathcal{L} .

We obtained the linking matrix in Fig. S3 by filling the m, n element of the matrix with the value of the linking number between the pair of loops with ID= m , n . We report results at $T=100$ K and at two different pressures (during compression), corresponding to LDA ($P=0.4$ GPa, panel A) and HDA ($P=1.6$ GPa, panel B). We note that in the linking matrix we do not observe

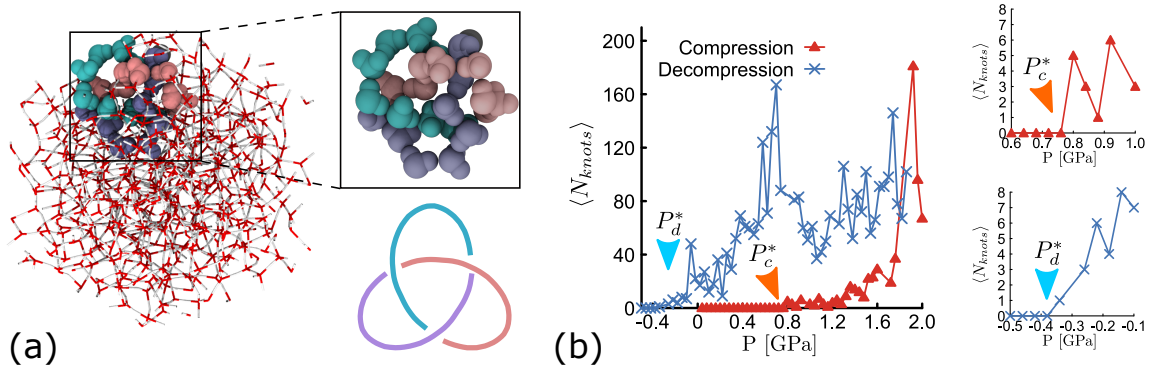


Figure S2. (a) Snapshot from simulations at $P = 2.0$ GPa. We found loops made up of exactly $l^* = 25$ water molecules. We restricted the search of loops to find up-to 500 000 loops passing through each vertex. We highlight an example of a trefoil knot found by our analysis and its corresponding idealized representation. (b) Left panel shows the average number of knots as a function of the pressure during compression and decompression. Right panels show a zoom-in to the results near the critical pressures P_c^* (top) and P_d^* (bottom).

elements with $|Lk| > 1$.

EXTENDED RESULTS

In fig. S4 we report $\langle \mathcal{L}/N_{loops} \rangle$ computed at higher temperatures compared to the main text. Panel A refers to $T=120$ K, while panel B refers to $T=140$ K.

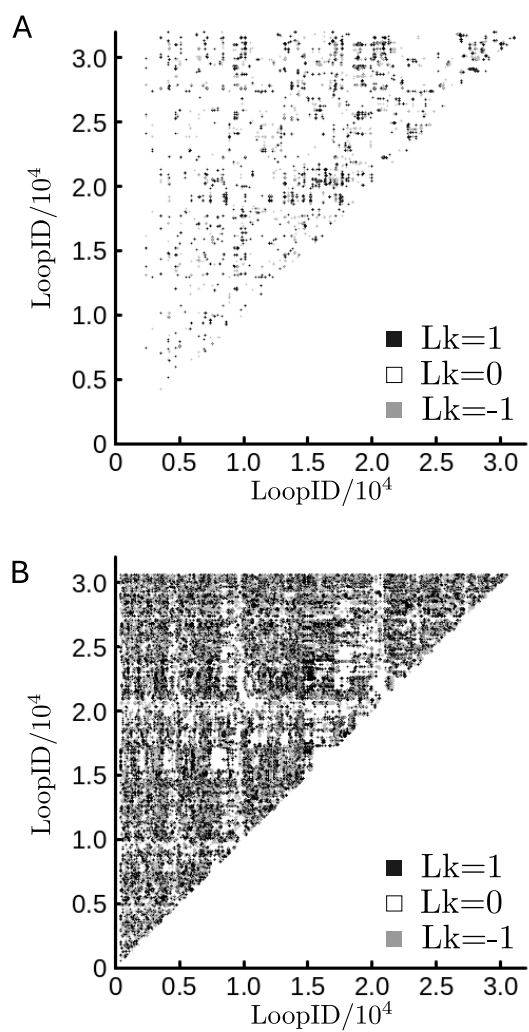


Figure S3. Linking matrix computed at $P=0.4$ GPa (A) and $P=1.6$ GPa (B).

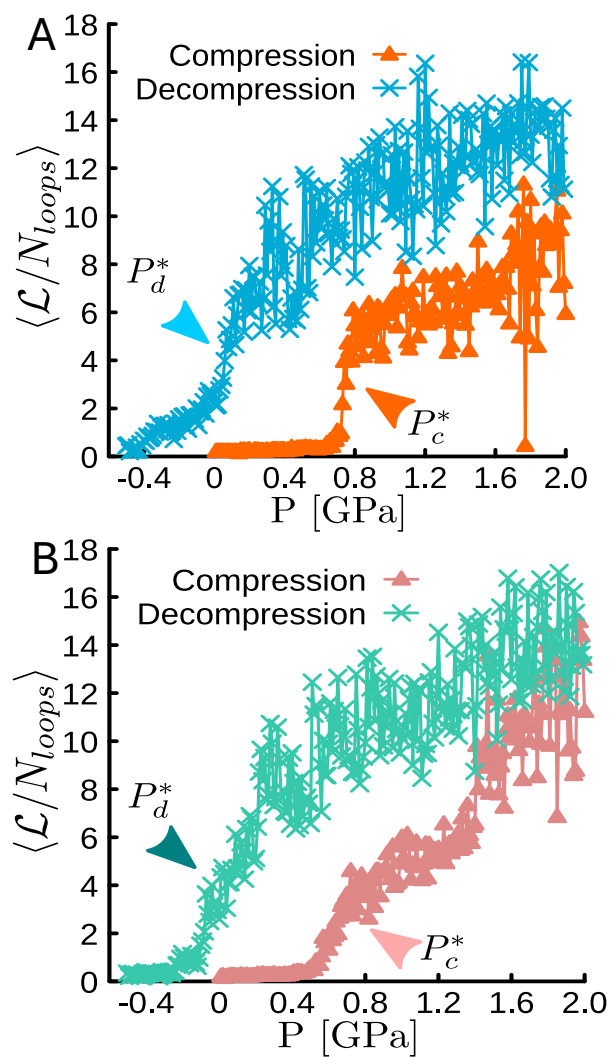


Figure S4. $\langle \mathcal{L}/N_{loops} \rangle$ computed during the compression/decompression cycles at $T=120$ K (A) and $T=140$ K (B).